

DESIGN AND VALIDATION OF SWITCHED MOVING BOUNDARY MODELING
FOR PHASE CHANGE THERMAL ENERGY STORAGE SYSTEMS

by

Trent J. Sakakini

APPROVED BY SUPERVISORY COMMITTEE:

Justin P. Koeln, Chair

Justin Ruths

Yaoyu Li

Copyright © 2023

Trent J. Sakakini

All rights reserved

*This thesis is dedicated
to my family and friends
for their continuous support
of my work*

DESIGN AND VALIDATION OF SWITCHED MOVING BOUNDARY MODELING
FOR PHASE CHANGE THERMAL ENERGY STORAGE SYSTEMS

by

TRENT J. SAKAKINI, BS

THESIS

Presented to the Faculty of
The University of Texas at Dallas
in Partial Fulfillment
of the Requirements
for the Degree of

MASTER OF SCIENCE IN
MECHANICAL ENGINEERING

THE UNIVERSITY OF TEXAS AT DALLAS

May 2023

ACKNOWLEDGMENTS

I would like to thank Dr. Justin P. Koeln for his guidance and support of my work throughout the years and for giving me an opportunity to learn the fundamentals of developing research. I would also like to thank Dr. Justin Ruths and Dr. Yaoyu Li for their willingness to assist with the thesis committee. I really appreciate the Energy Systems Control Laboratory group (Daniel Leister, Wenqing Wang, Vignesh Raghuraman, Alexander Gomez, David Gostin, and Juned Shaikh) and Alyssa Vellucci for their support of my work and helping throughout my research. I am thankful for my coaches (Danielle Kcholi and Aaron Capehart) and teammates (all, but specifically Griffin Davis, Joseph Kirby, Justin Ardis, Graeme Maclean, and Andres Uriegas) for their support and dedication to helping me run to heights that were unimaginable. A thanks to my family (Peter, Melissa, TJ, Trevor, and Tess Sakakini as well as Horace and Mary Cavitt) and Max Geller for their support and getting me to where I am today. Finally, I am grateful for Brynne Blackmar for her love and unwavering support of everything throughout the years.

May 2023

DESIGN AND VALIDATION OF SWITCHED MOVING BOUNDARY MODELING
FOR PHASE CHANGE THERMAL ENERGY STORAGE SYSTEMS

Trent J. Sakakini, MS
The University of Texas at Dallas, 2023

Supervising Professor: Justin P. Koeln, Chair

Thermal Energy Storage (TES) devices, which leverage the constant-temperature thermal capacity of the latent heat of a Phase Change Material (PCM), provide benefits to a variety of thermal management systems by decoupling the absorption and rejection of thermal energy. Control-oriented models are needed to predict the behavior of the TES to maximize the capabilities and efficiency of the overall system and experimental validation is needed to demonstrate the validity of the simplifying assumptions used to produce these control-oriented models. This thesis experimentally demonstrates the predictive capabilities of a switched Moving Boundary (MB) model that captures the key dynamics of the TES with significantly fewer states as compared to traditional approaches. A graph-based modeling approach is used to model the heat flow through the TES and the moving boundary captures the time-varying liquid and solid regions of the TES. A Finite State Machine (FSM) is used to switch between four different modes of operation based on the State-of-Charge (SOC) of the TES. The switched MB approach is shown to have similar accuracy and lower computational cost compared to traditional modeling approaches when predicting the SOC of an experimental TES device.

TABLE OF CONTENTS

ACKNOWLEDGMENTS	v
ABSTRACT	vi
LIST OF FIGURES	ix
LIST OF TABLES	xi
CHAPTER 1 INTRODUCTION	1
CHAPTER 2 MODELING	5
2.1 Graph-Based Modeling Framework	5
2.2 Fixed Grid TES Modeling Framework	7
2.2.1 Modeling Assumptions	7
2.2.2 Fixed Grid Approach	9
2.3 Proposed Switched Moving Boundary Modeling Framework	12
2.3.1 Moving Boundary Derivation	12
2.3.2 Moving Boundary Graph-Based Model	15
2.3.3 Finite State Machine	16
2.3.4 Incorporation of Natural Convection	18
2.3.5 Surface Area Ratio	19
CHAPTER 3 SIMULATION STUDY	21
3.1 Simulation Setup	21
3.2 Conduction-Only Heat Transfer	21
3.2.1 Complete Freezing and Melting	21
3.2.2 Partial Freeze-Melt Cycle	23
3.3 Final Proposed Model	24
3.3.1 Partial Freeze-Melt Cycle	24
CHAPTER 4 EXPERIMENTAL STUDY	26
4.1 Experimental Setup	26
4.1.1 Experimental System Overview	26
4.1.2 TES Description	27
4.1.3 Data Processing	27

4.2	Experimental Validation	30
4.2.1	Comparison of Mode 1	30
4.2.2	Complete Freeze-Melt Cycle	32
CHAPTER 5	CONCLUSIONS AND FUTURE WORK	35
REFERENCES	37
BIOGRAPHICAL SKETCH	40
CURRICULUM VITAE		

LIST OF FIGURES

2.1	Fixed Grid modeling framework. LEFT: Cylindrical TES with inner and outer walls and the PCM divided into n grid sections. TOP RIGHT: Identification of key radii used to model the 1-dimensional radial heat transfer. BOTTOM RIGHT: Graph-based FG model with n PCM vertices.	9
2.2	Computational comparisons of the FG and MB approaches. TOP: Time the model estimates for the PCM to completely freeze, t_{freeze} . MIDDLE: Computational time, t_{comp} . BOTTOM: Number of time steps taken with the ode23tb variable step solver, n_{steps} . All results are taken as an average over 50 simulations.	11
2.3	Simplified version of the PCM in the TES used to derive the MB model.	12
2.4	Proposed MB modeling framework. LEFT: Cylindrical TES with inner and outer walls and the PCM divided into solid and liquid regions, with states h_S and h_L , respectively. TOP RIGHT: Identification of key radii used to model the 1-dimensional radial heat transfer. BOTTOM RIGHT: Graph-based MB model with three vertices for the PCM.	15
2.5	FSM with switching criteria for the four modes of the MB model.	17
3.1	Differences between FG (with $n = 35$) and MB models for two complete freezing and melting cycles.	23
3.2	Differences between FG (with $n = 35$) and MB models for six partial freezing and melting cycles.	24
3.3	Differences between FG (with $n = 35$) and MB models for six partial freezing and melting switches. This MB model incorporates $\gamma = 2$ after the first switch.	25
4.1	Experimental system with core components labeled.	26
4.2	Diagram of the experimental VCS from Fig. 4.1 with three TES devices in series.	27
4.3	System configuration and flow directions for the charge (top figure) and discharge (bottom figure) modes of TES operation.	28
4.4	Sample images of TES with region tracing. LEFT: View of TES in freeze cycle. MIDDLE: The region in red is traced over the water-ice boundary from the left image. RIGHT: The region in red traces the copper pipe. This area is subtracted off from the ice area when the view of the copper pipe is obstructed by frost.	30
4.5	Comparison of the water temperature of the experimental system and the MB model while in Mode 1 of operation.	31
4.6	Differences between FG (with $n = 35$) and MB models for one complete freezing and melting cycle.	32

4.7	Comparison of the SOC from the experimental TES data, MB simulation, and FG simulation with images	33
4.8	Input temperatures for the complete freezing and melting cycle	34
4.9	Difference between using k_{eq} to account for natural convection in water to match experimental data compared to the conduction model presented in Section 3.2.1.	34

LIST OF TABLES

2.1	Power Flows for each FSM Mode	18
3.1	Simulation Parameters	22
4.1	System Components	29

CHAPTER 1

INTRODUCTION

The need for higher performance and more efficient thermal management systems has driven the design of systems with integrated Thermal Energy Storage (TES) devices that leverage the latent heat of a Phase Change Material (PCM). The design and performance of PCM-based TES has been well-studied (Nazir et al., 2019; Sharma et al., 2009; Zalba et al., 2003), resulting in a wide range of applications including building (Lee et al., 2020; Ma et al., 2012) and aircraft (Laird and Alleyne, 2021, 2019) thermal management, power electronics cooling (Pangborn et al., 2020), and combined heating and cooling (Bird and Jain, 2020).

Control-oriented models use simplifying assumptions to capture the key dynamic behaviors of complex systems, where experimental validation is necessary to assess the validity of these assumptions and ensure model accuracy. The broad field of energy management frequently uses control-oriented models for system analysis and control design (Ghaeminezhad et al., 2023; Chen and Wang, 2014; Agarwal et al., 2012). Within an energy management system, TES devices provide the ability to decouple the absorption and rejection of thermal energy, enabling better performance and efficiency. TES modeling approaches have been studied and model predictions have been validated through experimentation in applications such as building thermal management (Ma et al., 2012) and combined heat and power systems (Bird and Jain, 2020; Frazzica et al., 2022; Amagour et al., 2021).

The utility of a TES is heavily dependent on the dynamics associated with charging (where the PCM freezes from liquid to solid), discharging (where the PCM melts from solid to liquid), and strategic switching between these two modes of operation. Therefore, accurate control-oriented models of PCM-based TES are needed that capture their hybrid, nonlinear dynamics to be used in predictive controllers like Model Predictive Control (MPC), which have been developed for single-phase (Ma et al., 2012; Lee et al., 2020) and phase change (Pangborn et al., 2020) TES.

Traditional TES modeling approaches rely on dividing the PCM into multiple sections, where each section is modeled using a lumped-parameter approach. This Fixed Grid (FG) approach, also referred to as Finite Volume, is widely used in the literature (Shanks and Jain, 2022; Pangborn et al., 2015; Fasl and Alleyne, 2013) and is similar to a finite difference scheme (Fortunato et al., 2012). While this approach has proven to accurately model the complex dynamics of a TES device using relatively simple dynamics for each individual grid section, a large number of grid sections is needed to achieve this accuracy, resulting in a large number of dynamic states that is no longer practical for many control designs.

This thesis aims to develop and experimentally validate accurate control-oriented models of PCM-based TES devices using a graph-based switched Moving Boundary (MB) approach. Graph-based modeling (Wang and Koeln, 2020; Laird and Alleyne, 2021, 2019; Pangborn et al., 2020; Shanks and Jain, 2022) is used to develop both FG and MB models, where a graph is used to clearly identify the underlying structure of thermal energy storage and heat transfer throughout the TES device. While the FG model divides the PCM into n sections, each with its own dynamic enthalpy state, the proposed MB approach only requires three states corresponding to the enthalpies of the solid and liquid regions of the PCM and the overall State-of-Charge (SOC), defined as the mass of the solid portion compared to the total mass of the PCM.

Several MB approaches to TES modeling have recently been proposed (Fasl and Alleyne, 2013; Laird and Alleyne, 2019; Pangborn et al., 2020) but each has limitations. Specifically, the TES devices modeled in both (Laird and Alleyne, 2019) and (Fasl and Alleyne, 2013) are limited to operation where heat flows in only one direction through the PCM, i.e., heat always enters on one side and exits on the other. However, many TES devices operate by exchanging heat with a single working fluid flowing through the center of the TES. The TES model developed in (Pangborn et al., 2020) captures how a heat transfer effectiveness coefficient for the PCM is a function of SOC and the mode of operation (charging or discharging) but modeling the completely melted or solidified modes of operation is left for future work.

The proposed switched MB approach overcomes these limitations using a Finite State Machine (FSM) to model the mode-dependent dynamics associated with freezing, melting, completely solid, and completely liquid operation. A similar FSM is used to model the operation of ultracapacitors (Dede et al., 2016). When compared to the FG model in a simulated example, the proposed switched MB model achieves a maximum error of 5% for the SOC of the PCM with a 80% reduction in computational time. Therefore, the primary contribution of this thesis is the specific formulation of a graph-based switched MB model that is able to accurately predicted the key dynamics of PCM-based TES devices with far fewer states when compared to a more traditional FG model.

The final proposed model accounts for the improved heat transfer due to natural convection in the liquid region of the PCM. Natural convection within the annulus of two concentric cylinders has been thoroughly investigated. In the work by Kuehn and Goldstein (Kuehn and Goldstein, 1976), natural convection is studied at steady-state for air and water with numerical and experimental approaches across a large range of Rayleigh numbers ($10^2 \leq Ra \leq 10^6$). The average effects of natural convection were modeled by identifying a mean equivalent conductivity coefficient (k_{eq}) that captures the increased heat transfer due to natural convection compared to pure conduction. Wang et al. (Wang et al., 2019) extend this approach to different geometries with a cylinder encapsulating different internal regular polygon-shaped tubes for $Ra > 5 \times 10^4$. Additional numerical and experimental studies are presented in (Zhang et al., 2014) and (Francis et al., 2002) that provide relationships between k_{eq} and Ra for water and air.

The main contribution of this thesis is an experimentally validated graph-based switched MB model that accurately predicts the key dynamics of PCM-based TES devices. Specific elements of this contribution include: (1) the development of a graph-based switched MB model for phase change TES; (2) incorporation of k_{eq} to account for effects of natural convection; (3) a surface area correction factor that improves model accuracy for partial freezing

and melting operation producing multiple solid and liquid regions; and (4) experimental data and images from a water-based TES used to validate the proposed modeling approach.

The remainder of the thesis is organized as follows. Chapter 2 introduces and motivates the graph-based modeling framework and then uses graph-based modeling to develop a traditional FG and the proposed switched MB models of a TES device. Simulation comparisons between the FG and MB models are presented and discussed in Chapter 3. Chapter 4 describes the experimental system used to validate the switched MB model and presents experimental data that shows the high degree of accuracy achieved by the proposed switched MB model. Finally, conclusions and future work are summarized in Chapter 5.

CHAPTER 2

MODELING

2.1 Graph-Based Modeling Framework

This thesis employs graph-based modeling, similar to (Wang and Koeln, 2020), to capture the storage and transfer of energy in PCM-based TES devices. Specifically, Fig. 2.1 shows the graph-based model using the FG approach for a cylindrical TES device.

This TES device consists of two concentric cylindrical pipes, where the PCM is encapsulated between the inner and outer pipes. A working fluid flows through the inner pipe with an inlet temperature T_{in} and is the main mechanism in which heat is transferred between the TES device and the remainder of the overall thermal management system (which is not modeled in this work). The outer wall of the outer pipe is assumed to exchange heat with ambient air at temperature T_{air} . In the FG approach, the PCM is divided to n grid sections, where the i^{th} grid section is assumed to have a uniform enthalpy h_i . This thesis only considers the radial heat transfer of the TES device and assumes uniform behavior along the length of the device L . While the proposed approach is intended to extend to TES of different geometries, only the cylindrical shape is considered in this thesis.

When capturing the structured dynamics of a system, a graph consists of a set of N_v dynamic vertices $V = \{v_i : i \in [1, N_v]\}$, representing energy stored by capacitive sections of a system, and a set of N_e edges $E = \{e_j : j \in [1, N_e]\}$, representing power flows among these capacitive sections. Note that $[1, N_v]$ is used to denote the set of integers between 1 and N_v . Each edge e_j has an orientation denoting the direction of positive power flow P_j from the tail vertex v_j^{tail} to the head vertex v_j^{head} . Based on conservation of energy, the energy stored by i^{th} vertex v_i (quantified by the dynamic state x_i) can be expressed as

$$C_i \dot{x}_i = \sum_{e_j \in E_i^{in}} P_j - \sum_{e_j \in E_i^{out}} P_j, \quad (2.1)$$

where C_i is the energy storage capacitance while E_i^{in} and E_i^{out} are the set of edges directed into and out of vertex v_i . Generally, in a graph-based modeling framework, the power flow P_j is constrained to be a function of an associated input \tilde{u}_j and the state of the tail and head vertices, x_j^{tail} and x_j^{head} , such that

$$P_j = f_j(x_j^{tail}, x_j^{head}, \tilde{u}_j). \quad (2.2)$$

In general, the graph-based modeling framework allows for power to enter the system along source edges. For the TES device shown in Fig. 2.1, there are two sources into the system: heat transfer with the main working fluid (wf) and with the surrounding air.

For heat that is being transferred out of the system, a sink vertex denoted $V^{out} = \{v_i^{out} : i \in [1, N_v^{out}]\}$ is included in the graph. This vertex has an associated state x_i^{out} that serves as the outlet of the working fluid.

The structure of the graph, including both the dynamic vertices and sink vertices, is captured by the incidence matrix $M = [m_{ij}] \in \mathbb{R}^{(N_v + N_v^{out}) \times N_e}$ defined as

$$m_{ij} = \begin{cases} +1 & \text{if } v_i \text{ is the tail of } e_j, \\ -1 & \text{if } v_i \text{ is the head of } e_j, \\ 0 & \text{else.} \end{cases} \quad (2.3)$$

The incidence matrix is partitioned based on dynamic and sink vertices such that

$$M = \begin{bmatrix} \bar{M} \\ \underline{M} \end{bmatrix} \quad \text{with } \bar{M} \in \mathbb{R}^{N_v \times N_e}, \quad (2.4)$$

where the indexing of vertices is assumed to be ordered such that \bar{M} is a structural mapping from power flows

$$P = F(x, x^{out}, \tilde{u}) = [f_j(x_j^{tail}, x_j^{head}, \tilde{u}_j)], \quad (2.5)$$

to states $x = [x_i]$, $i \in [1, N_v]$, and \underline{M} is a structural mapping from P to sink states $x^{out} = [x_i^{out}]$, $i \in [1, N_v^{out}]$. Combining the individual conservation equations from (2.1) using the

structure of the graph captured by \bar{M} , the overall system dynamics are

$$C\dot{x} = -\bar{M}P = -\bar{M}F(x, x^{out}, \tilde{u}), \quad (2.6)$$

where $C = \text{diag}([C_i])$, $i \in [1, N_v]$ is a diagonal matrix of capacitances. Since some edges do not have a control input and a single input can affect multiple edges, it is often advantageous to let $\tilde{u} \in \mathbb{R}^{N_e}$ be a virtual input vector, corresponding to the N_e edges, and define $u \in \mathbb{R}^{N_u}$ as a system input vector, corresponding to the subset of N_u unique inputs that affect the system. As such, the matrix $\Phi \in \mathbb{R}^{N_e \times N_u}$ can be used to map the system inputs to the virtual inputs such that $\tilde{u} = \Phi u$.

One benefit of a graph-based modeling framework is that the linear structure of the graph is captured by (2.6) and the majority of the modeling effort focuses on defining the potentially nonlinear power flow relationships in (2.5). The following sections presents the graph capturing the structure of the systems shown in Figs. 2.1 and 2.4, with the vertex and edge properties used to model the dynamics.

2.2 Fixed Grid TES Modeling Framework

2.2.1 Modeling Assumptions

The modeling framework is developed through a conductive heat transfer approach and is used with the addition of k_{eq} to account for natural convection, which will be discussed in Section 2.3.4. The dynamics of the TES, comprised of the working fluid, inner wall, PCM, and outer wall, are modeled using a graph-based framework with the following assumptions.

1. Heat transfer within the TES is radially symmetric and uniform along the length of the device.
2. Conductive heat transfer is assumed throughout the TES except for the liquid region of the PCM where k_{eq} is used to capture the net effects of natural convection.

3. The mass in the PCM is assumed to be constant with time-varying volume based on the density changes associated with phase change.
4. Heat transfer between the working fluid and the inner pipe is governed by the outlet temperature of the working fluid.
5. All material properties are phase dependent but constant within each phase.
6. The pressure of the PCM is assumed to be constant over time, space, and phase and does not influence the TES dynamics.

The following graph-based models use enthalpies as system states, since temperature cannot be used to quantify thermal energy during phase change. The PCM is generically assumed to have a saturated solid state enthalpy of $h = 0 \text{ kJ/kg}$, a latent heat of fusion of h_f , and a saturated temperature of T_{sat} .

Temperature T for the PCM is defined as

$$T = \begin{cases} \frac{h}{C_{p,\sigma}} + T_{sat} & \text{if } h < 0, \\ T_{sat} & \text{if } 0 \leq h \leq h_f, \\ \frac{h-h_f}{C_{p,\sigma}} + T_{sat} & \text{if } h > h_f, \end{cases} \quad (2.7)$$

where $C_{p,\sigma}$ is the phase-dependent specific heat capacity of the PCM and the phase σ , either solid (S) or liquid (L), is

$$\sigma = \begin{cases} S & \text{if } T < T_{sat}, \\ L & \text{if } T \geq T_{sat}. \end{cases} \quad (2.8)$$

For single-phase materials, such as the working fluid and the pipe walls, temperature is defined as $T = \frac{h}{C_p}$, where C_p is the specific heat capacity of the material.

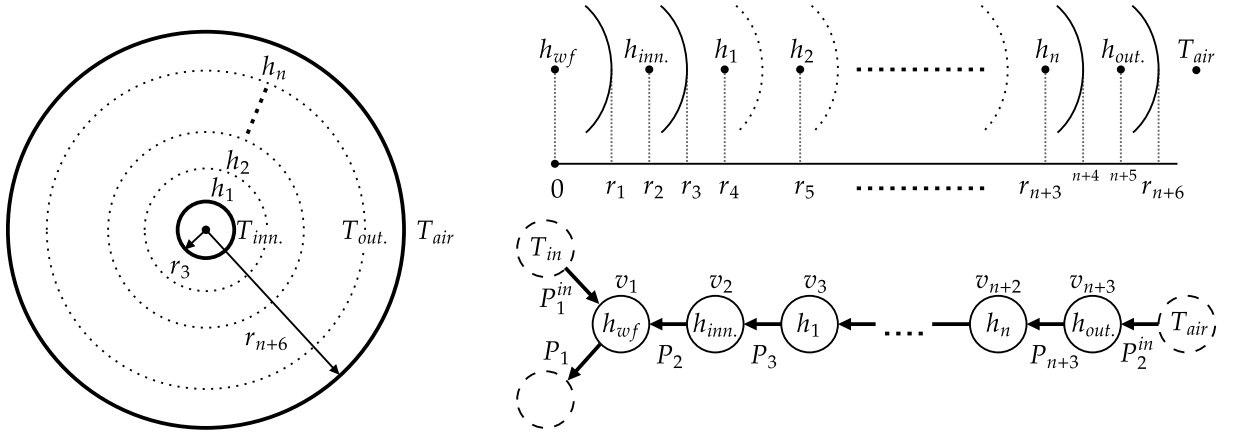


Figure 2.1. Fixed Grid modeling framework. LEFT: Cylindrical TES with inner and outer walls and the PCM divided into n grid sections. TOP RIGHT: Identification of key radii used to model the 1-dimensional radial heat transfer. BOTTOM RIGHT: Graph-based FG model with n PCM vertices.

2.2.2 Fixed Grid Approach

The traditional FG approach to modeling PCM-based TES devices divides the volume into n grid sections (Shanks and Jain, 2022; Fasl and Alleyne, 2013). The FG modeling framework is used as a reference in this thesis, which will be used as a comparison for the proposed switched MB approach in addition to the experimental system.

As shown in Fig. 2.1, the FG approach requires a total of $n+3$ states such that $x \in \mathbb{R}^{n+3}$, where $x = [h_{wf}, h_{inn.}, h_1, \dots, h_n, h_{out.}]^T$ are the enthalpies of the working fluid, the inner wall, the n sections of PCM, and the outer wall.

The following graph-based FG model is derived from the approach presented in (Fasl and Alleyne, 2013) and the radial heat transfer equations from (Bergman and Incropera, 2011). Modeling each vertex in Fig. 2.1 using conservation of energy, with state h_i for the i^{th} vertex, the energy storage capacitance C_i from (2.1) is the mass of the vertex such that $C_i = \rho_i V_i$ for the single-phase material vertices $i \in \{1, 2, n+3\}$ and $C_i = \rho_{i,\sigma} V_i$ for the PCM vertices $i \in \{3, n+2\}$. The density ρ_i is assumed constant for single-phase materials while $\rho_{i,\sigma}$ denotes the fact that the PCM density is phase-dependent. The volumes V_i for the three

single-phase vertices are defined as $V_1 = \pi L r_1^2$, $V_2 = \pi L (r_3^2 - r_1^2)$, and $V_{n+3} = \pi L (r_{n+6}^2 - r_{n+4}^2)$, based on the radii labelled in Fig. 2.1, where L is the length of the TES device. The PCM is divided into n sections of equal width $\Delta r = \frac{r_{n+4} - r_3}{n}$ such that the volumes V_i , $i \in [3, n+2]$, are defined as $V_i = \pi L [(r_{i+1} + \frac{\Delta r}{2})^2 - (r_{i+1} - \frac{\Delta r}{2})^2]$.

Each power flow P_j can be expressed in the form of (2.2) assuming positive power flow in the direction of the arrows shown in Fig. 2.1. The advective power flows associated with the working fluid are $P_1^{in} = \dot{m}_{wf} C_{p,wf} T_{in}$ and $P_1 = \dot{m}_{wf} C_{p,wf} T_1$, where \dot{m}_{wf} is the mass flow rate and $C_{p,wf}$ is the specific heat capacity of the working fluid. For heat transfer from the surrounding air into the TES, the outer wall is a combination of the pipe material and insulation,

$$\begin{aligned} P_2^{in} &= \frac{1}{R_{out.} + R_{air}} (T_{air} - T_{n+3}), \\ R_{out.} &= \frac{\ln(\frac{r_{n+6}}{r_{n+5}})}{2\pi L k_{out.}}, R_{air} = \frac{1}{2\pi r_{n+6} L h_{air}}, \end{aligned} \quad (2.9)$$

where $k_{out.}$ is the thermal conductivity of the outer pipe and h_{air} is the convective heat transfer coefficient for the air, which will be determined experimentally. Power flows within the PCM are derived using a conduction-only approach, where effects due to natural convection are accounted for in Section 2.3.4. For power flows P_j , $j \in [2, n+3]$,

$$P_j = \frac{1}{R_j} (T_j - T_{j-1}). \quad (2.10)$$

Since each power flow P_j , $j \in [2, n+3]$, goes through two different materials, the total thermal resistance is defined as $R_j = R_{j,A} + R_{j,B}$, where $R_{2,A} = \frac{1}{2\pi r_1 L h_{wf}}$, $R_{2,B} = \frac{\ln(\frac{r_2}{r_1})}{2\pi L k_{inn.}}$, $R_{3,A} = \frac{\ln(\frac{r_3}{r_2})}{2\pi L k_{inn.}}$, $R_{n+3,B} = \frac{\ln(\frac{r_{n+5}}{r_{n+4}})}{2\pi L k_{out.}}$, and, $\forall j \in [3, n+2]$,

$$R_{j,B} = \frac{\ln(\frac{r_{j+1}}{r_{j+1} - \frac{\Delta r}{2}})}{2\pi L k_{j,\sigma}}, R_{j+1,A} = \frac{\ln(\frac{r_{j+1} + \frac{\Delta r}{2}}{r_{j+1}})}{2\pi L k_{j,\sigma}}, \quad (2.11)$$

where $k_{inn.}$ is the thermal conductivity of the inner pipe and h_{wf} is the convective heat transfer coefficient for the working fluid.

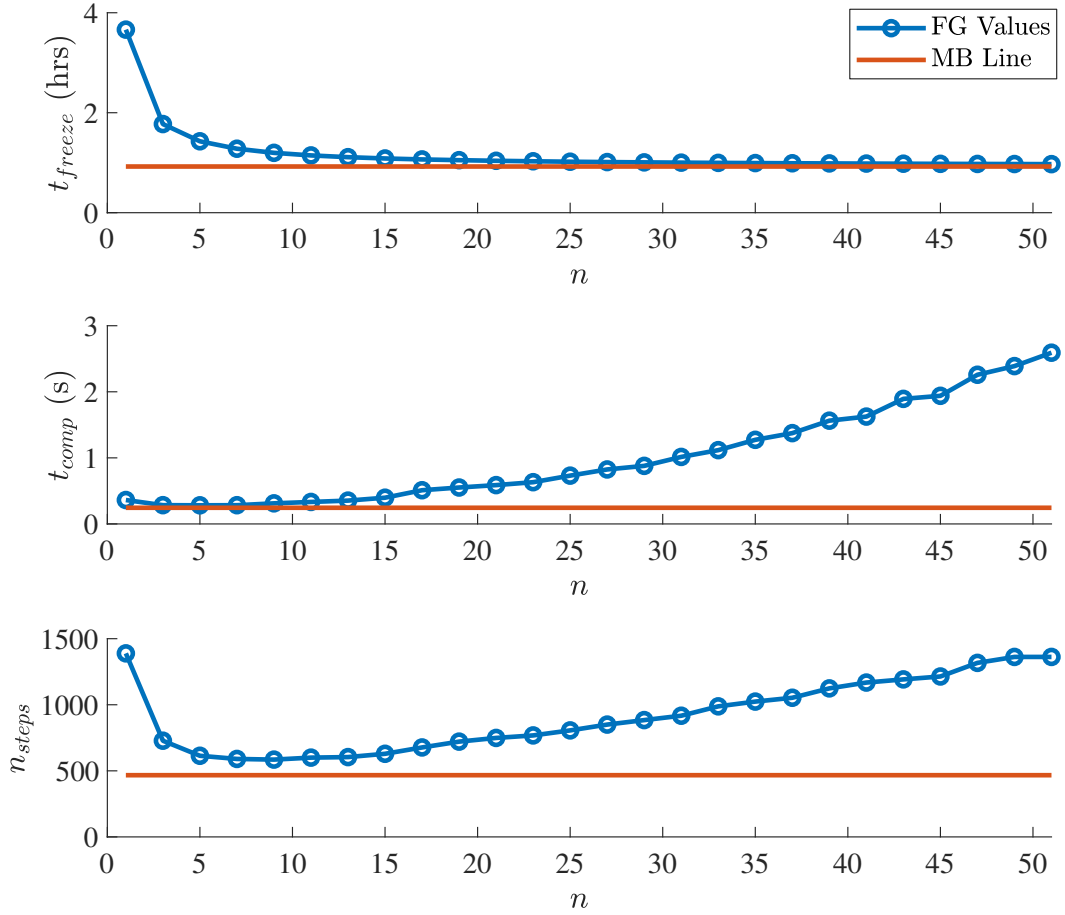


Figure 2.2. Computational comparisons of the FG and MB approaches. TOP: Time the model estimates for the PCM to completely freeze, t_{freeze} . MIDDLE: Computational time, t_{comp} . BOTTOM: Number of time steps taken with the ode23tb variable step solver, n_{steps} . All results are taken as an average over 50 simulations.

For the numerical examples presented in Chapters 3 and 4, Fig. 2.2 shows the results of a series of tests to determine the behavior of the FG model as a function of n . The top plot shows the simulated time required to completely freeze the TES, t_{freeze} , for different values of n . While t_{freeze} converges for increasing n , the second plot shows the associated increase in computation time for the simulation, t_{comp} . These simulations were conducted in MATLAB Simulink using the variable step solver ode23tb. The third plot shows that the increase in computation time is due to an increasing number of states and simulation time steps. Based on the results of Fig. 2.2, $n = 35$ sections was chosen for comparison with the

proposed switched MB approach presented in the following section for the FG model as a practical balance of model accuracy and computational cost.

2.3 Proposed Switched Moving Boundary Modeling Framework

2.3.1 Moving Boundary Derivation

The MB approach aims to capture the primary dynamics of the TES with a reduced number of states to be used for system analysis and control design.

For the MB model, the PCM in the TES is divided into three regions: solid, liquid, and the interface inbetween. The dynamics associated with each region are derived individually, then combined within the graph-based modeling framework. A simplified version of the PCM in the TES is used to derive these dynamics, as shown in Fig. 2.3. The power flows between each region are represented by P , where subscripts S and L denote power flows for the solid and liquid regions, respectively, and subscripts i and o denote power flows going into or out of the solid and liquid regions, respectively. The heat flow direction is assumed to go from the liquid region to the solid region, as that is the main direction of heat flow during the freezing process of the TES.

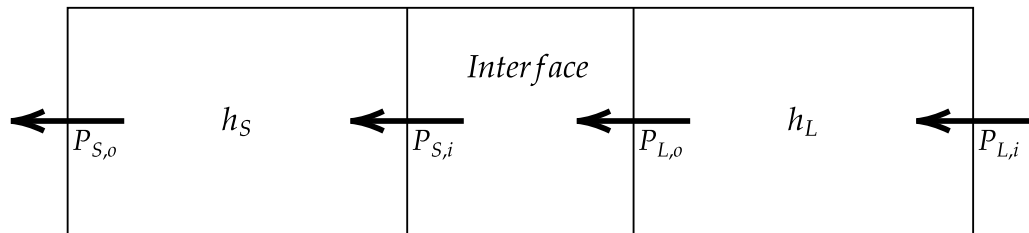


Figure 2.3. Simplified version of the PCM in the TES used to derive the MB model.

State of Charge Definition

The SOC is defined as the solid mass fraction of the PCM in the TES ($0 \leq SOC \leq 1$). The TES is assumed to only have either solid or liquid PCM, so the definitions of mass can be defined as,

$$\begin{aligned} M_S &= M_{tot}SOC, \\ M_L &= M_{tot}(1 - SOC), \end{aligned} \tag{2.12}$$

where M_S is the mass of solid PCM, M_L is the mass of liquid PCM, and M_{tot} is the total mass of the PCM in the TES.

Interface Region

The interface region is assumed to be the boundary between the solid and liquid regions of the PCM. For this region, it is assumed that there is no mass or energy stored. For example, all mass lost by the liquid region due to the freezing of the PCM is instantaneously gained by the solid region, and vice versa when the PCM is melting. Therefore, the interface region is treated as a static vertex in a graph-based modeling framework, where algebraic versions of conservation of mass and conservation of energy are applied.

Conservation of energy applied to the interface region results in

$$0 = P_{L,o} + \dot{m}_i h_L - P_{s,i} - \dot{m}_i h_S, \tag{2.13}$$

where \dot{m}_i is the mass flow rate PCM mass through the interface region. The convective heat transfer between the liquid region and the interface is modeled as $P_{L,o}$, while the conductive heat transfer between the interface and the solid region is modeled as $P_{s,i}$. The heat transfer due to advection from the liquid into the interface is $\dot{m}_i h_L$, while the heat transfer due to advection from the interface to the solid is $\dot{m}_i h_S$. Because both solid and liquid regions have the same mass flow rate, $\dot{m}_i = \dot{M}_S = -\dot{M}_L$ is used. Taking the derivatives of (2.12) with

respect to SOC results in,

$$\begin{aligned}\dot{M}_S &= M_{tot}\dot{SOC}, \\ \dot{M}_L &= -M_{tot}\dot{SOC}.\end{aligned}\tag{2.14}$$

Finally, the dynamics of the interface region, which capture the rate of change of SOC, come from combining (2.13) and (2.14) and rearranging to get,

$$(h_S - h_L)M_{tot}\dot{SOC} = P_{L,o} - P_{s,i}.\tag{2.15}$$

Solid Region

The solid region is modeled using conservation of energy to determine the dynamics of h_S , which represents the lumped enthalpy of the solid PCM. Setting the rate of change of energy stored in the solid region equal to the power flows into and out of the region results in

$$\dot{M}_S h_S + M_S \dot{h}_S = P_{S,i} - P_{S,o} + \dot{m}_i h_S,\tag{2.16}$$

where the left-hand side comes from taking the derivative of $M_S h_S$ (the energy stored in the solid region). Combining (2.12) and (2.16) and further simplifying results in,

$$M_{tot}SOC\dot{h}_S = P_{S,i} - P_{S,o}.\tag{2.17}$$

Liquid Region

The liquid region is treated similarly to the solid region, where applying conservation of mass results in

$$\dot{M}_L h_L + M_L \dot{h}_L = P_{L,i} - P_{L,o} - \dot{m}_i h_L,\tag{2.18}$$

where the left-hand side comes from taking the derivative of $M_L h_L$ (the energy stored in the liquid region). Combining (2.12) and (2.18) and further simplifying results in,

$$M_{tot}(1 - SOC)\dot{h}_L = P_{L,i} - P_{L,o}.\tag{2.19}$$

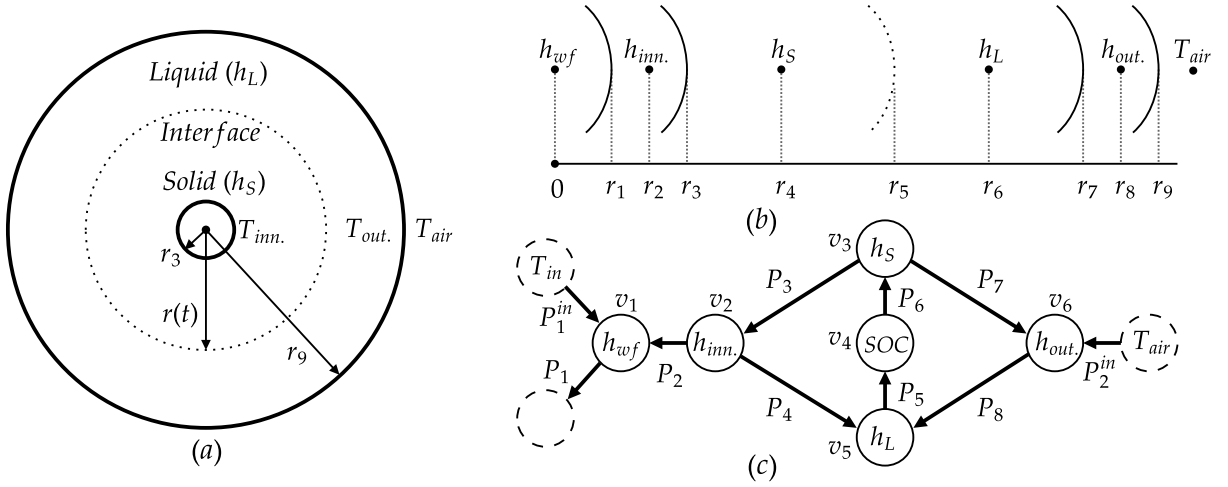


Figure 2.4. Proposed MB modeling framework. LEFT: Cylindrical TES with inner and outer walls and the PCM divided into solid and liquid regions, with states h_S and h_L , respectively. TOP RIGHT: Identification of key radii used to model the 1-dimensional radial heat transfer. BOTTOM RIGHT: Graph-based MB model with three vertices for the PCM.

2.3.2 Moving Boundary Graph-Based Model

As shown in Fig. 2.4, the proposed MB approach requires a total of six states such that $x \in \mathbb{R}^6$, where $x = [h_{wf}, h_{inn.}, h_S, SOC, h_L, h_{out.}]^T$ has only three PCM states corresponding to the SOC and enthalpies of the solid (h_S) and liquid (h_L) regions of the PCM, derived from the dynamic states in (2.15), (2.17), and (2.19), respectively. This can be significantly fewer states than the FG approach which requires $n + 3$ states, where $n = 35$ was determined to be a practical balance between model accuracy and computational cost.

Since the MB model only changes the configuration of the PCM, power flows P_j , $j \in \{1, 2\}$, power inputs P_j^{in} , $j \in \{1, 2\}$, capacitances C_i , $i \in \{1, 2, 6\}$, and resistances $R_{j,A}$, $j \in \{1, 2, 3\}$ and $R_{j,B}$, $j \in \{1, 2\}$ are all the same for the working fluid, and the inner and outer wall as defined in the FG model, by replacing v_{n+3} in the FG with v_6 in the MB.

Modeling the three new vertices in Fig. 2.4 using conservation of energy, equations (2.15), (2.17), and (2.19) can be manipulated to obtain the energy storage capacitance C_i , similar to (2.1), as the mass of the vertex such that $C_3 = M_{tot}SOC$, $C_4 = M_{tot}(h_S - h_L)$, and

$C_5 = M_{tot}(1 - SOC)$, where (2.12) can be manipulated to define $SOC = \frac{M_S}{M_{tot}}$ as the solid mass fraction of the PCM in the TES.

While capacitances are typically positive in a graph-based modeling framework, $C_4 < 0$ since $h_S < h_L$, which comes directly from the fact that the state, $x_4 = SOC$, increases with a decrease in energy stored in the PCM such that $SOC = 0$ and $SOC = 1$ correspond to the PCM being completely liquid and completely solid, respectively.

The power flow P_j , $j \in [3, 8]$, are defined similarly to (2.10), such that power flow is driven by the temperature difference between the tail and head vertex temperatures for each edge. Note that T_{sat} is used as the vertex temperature for v_4 with the state corresponding to SOC. The total thermal resistance is still defined as $R_j = R_{j,A} + R_{j,B}$, but now the radii associated with the solid and liquid regions are time varying. For example, as shown in Fig. 2.4, $r_5 = \sqrt{r_3^2 + \frac{M_S}{\rho_S \pi L}}$.

The following section shows how a FSM is used to turn on and off power flows in Fig. 2.4 to accurately model the dynamics of the TES device under four distinct modes of operation.

2.3.3 Finite State Machine

The TES device has four major modes of operation: completely liquid, completely solid, freezing, and melting modes, as shown in Fig. 2.5 with their respective mode numbers. Mode switching is based on the SOC and the surface temperature (T_{s_i}) between the inner pipe wall ($T_{inn.}$) and the PCM, defined as

$$T_{s_i} = \begin{cases} T_{inn.} + R_{3,A}P_3 & \text{if } Mode \in \{2, 3\}, \\ T_{inn.} + R_{4,A}P_4 & \text{if } Mode \in \{1, 4\}. \end{cases} \quad (2.20)$$

Assuming the PCM starts in a completely liquid state (Mode 1), when the inlet working fluid temperature $T_{in} < T_{sat}$ eventually $T_{s_i} < T_{sat}$ and the freezing process begins, switching the model into Mode 2 of the FSM. During the freezing process, the SOC will increase until

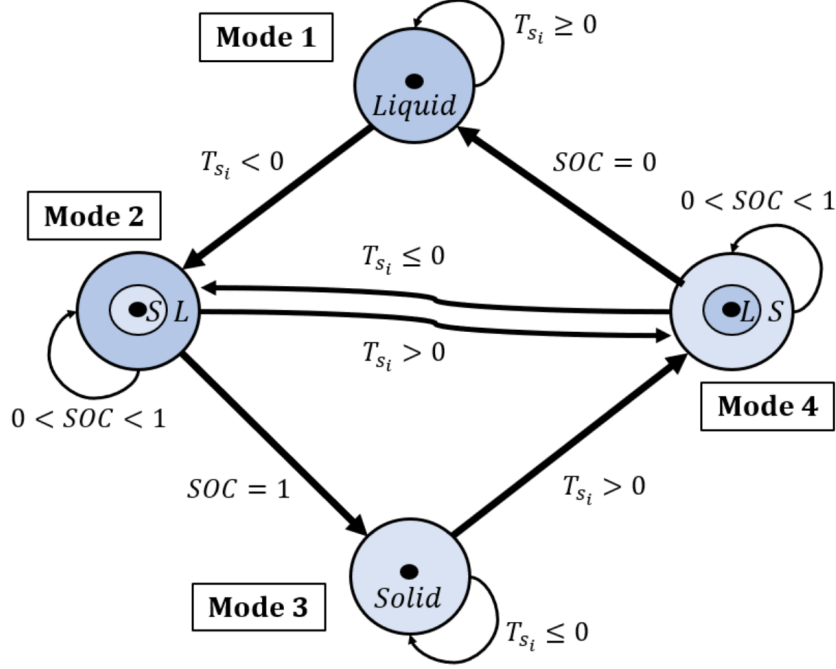


Figure 2.5. FSM with switching criteria for the four modes of the MB model.

the PCM is completely solid where $SOC = 1$ and the model switches to Mode 3. If the inlet working fluid temperature increases such that $T_{in} > T_{sat}$, then eventually $T_{si} > T_{sat}$, and the melting process begins by switching to Mode 4. Once the PCM is completely liquid, where $SOC = 0$, the model switches back into Mode 1. If the inlet working fluid temperature changes when the system is in Modes 2 or 4 before completely freezing or melting, the model can switch directly between Modes 2 and 4 with the PCM in a partially frozen state. During such transitions, note that the model makes a non-physical assumption that locations of the solid and liquid regions instantaneously switch such that solid is surrounded by liquid in Mode 2 and vice versa in Mode 4, as shown in Fig. 2.5. While the SOC state still evolves continuously, the radii associated with the solid and liquid regions will change instantaneously to reflect the mode switch.

While the graph in Fig. 2.4 shows all of the potential power flows through the PCM, power flows P_3 through P_8 are turned on and off based on the mode of operation as summarized in Table 2.1. For example, when the PCM is completely liquid (Mode 1), power flows P_3 , P_5 ,

Table 2.1. Power Flows for each FSM Mode

Power Flow	Mode 1	Mode 2	Mode 3	Mode 4
P_3	off	on	on	off
P_4	on	off	off	on
P_5	off	on	off	on
P_6	off	on	off	on
P_7	off	off	on	on/off*
P_8	on	on	off	off/on*

* Switching in Mode 4 dependent on the enthalpy of the solid region, as described in Section 2.3.3.

P_6 , and P_7 are all turned off to completely disconnect vertices v_3 and v_4 and allow both the inner and outer walls to exchange heat with only the liquid, vertex v_5 .

For Mode 4, it is possible for liquid PCM to form next to the outer wall due to heat transfer with the outer wall and the ambient air. To ensure the solid region stays below the two-phase region, power flow switching is incorporated while Mode 4 is in operation. Therefore, within Mode 4, either P_7 or P_8 is turned on, but never both, where P_7 is on if $h_S \leq 0$.

Finally, the radii labeled in Fig. 2.4 only correspond to Mode 2 of the FSM and are used in computing the thermal resistances $R_{j,A}$ and $R_{j,B}$. For the other three modes, the equations for these thermal resistances must be modified to reflect the geometry and corresponding radii for each mode.

2.3.4 Incorporation of Natural Convection

Mean equivalent conductivity coefficient (k_{eq}) is a factor that scales conductive heat transfer to account for the effects of natural convection in a fluid, determined by the Rayleigh number (Ra) (Kuehn and Goldstein, 1976; Francis et al., 2002). The power flow accounting for conduction and natural convection is $P = k_{eq}P_{Cond}$, where P_{Cond} is the conduction-only heat transfer modeled using (2.10). For an annulus between concentric cylinders, the Rayleigh

numbers for the inner and outer cylinders are

$$Ra_{Di} = \frac{\beta g(T_{inn.} - T_L) D_i^3}{(\alpha \nu)}, \quad (2.21)$$

$$Ra_{Do} = \frac{\beta g(T_L - T_{out.}) D_o^3}{(\alpha \nu)}, \quad (2.22)$$

where β is the thermal expansion coefficient, α is the thermal diffusivity, ν is the kinematic viscosity of the fluid, and D_i and D_o are the inner and outer diameters, respectively. The Rayleigh number to use is dependent on the location of the PCM in liquid-state, where Ra_{Di} is used in Modes 1 and 4, Ra_{Do} is used in Mode 2, and Mode 3 does not use Ra as there is only solid-state PCM.

Relationships between Ra and k_{eq} are shown in (Kuehn and Goldstein, 1976; Wang et al., 2019; Zhang et al., 2014) and can be used to estimate the effects of natural convection. Conduction is the dominating heat transfer mechanism when $Ra \leq 2 \times 10^4$, which corresponds to $k_{eq} = 1$. Convection dominated heat transfer happens when $Ra \geq 5 \times 10^4$ and (Kuehn and Goldstein, 1976) gives the power law correlation $k_{eq} = 0.202 Ra^{0.25}$ for water, which is used in the following simulations for the FG and MB models. While the proposed PCM model is intended to be used for any two-phase material, experimentation is necessary to find the power law correlation of k_{eq} for other PCMs.

2.3.5 Surface Area Ratio

For the partial freezing and melting cases, the MB model only has one state each for the solid and liquid regions. This limitation makes it difficult to model a series of concentric rings of solid and liquid PCM that may form in the TES. Alternatively, the FG model is capable of modeling this behavior assuming n is chosen large enough to accurately represent these rings of alternating phase.

The Shape Factor, S , is used in conductive heat transfer applications to develop relatively simple models of the overall heat transfer between two solids with complex geometries

(Bergman and Incropera, 2011). Inspired by this approach, a surface area ratio, γ , is used as a geometric scaling factor for P_5 and P_6 , which connect the SOC vertex to the liquid and solid enthalpy vertices, respectively. In the proposed MB model, when multiple solid and liquid regions would be formed, the increase in surface area between regions is accounted for by γ . The surface area ratio $\gamma \neq 1$ is applied when switching directly from Mode 2 to 4, or vice versa, with the potential to account for multiple solid or liquid regions. A switch to Modes 1 or 3 resets $\gamma = 1$. For the simulation results in Section 3, $\gamma = 2$ is used when switching directly from Mode 2 to 4, or vice versa, to show the benefits of accounting for partial freezing and melting. However, allowing γ to be a function of SOC such that $\gamma(SOC)$ may provide additional model accuracy improvements and is the focus of future work.

CHAPTER 3

SIMULATION STUDY

3.1 Simulation Setup

Table 3.1 shows the simulation parameters used to compare the MB model to the experimental system and the more traditional FG model. The material properties for the simulated TES device assume that R-134a is the working fluid, the inside pipe is copper (*Cu*), the PCM is water, and the outer pipe is Tygon PVC to match the components on the experimental system that will be compared to in Section 4.

While *SOC* is a state of the MB model, for the FG model, *SOC* is computed as

$$SOC_{FG} = \frac{1}{M_{tot}} \sum_{j=3}^{n+2} C_j \left(1 - \frac{\max(0, \min(h_j, h_f))}{h_f} \right). \quad (3.1)$$

To compare the *SOC* for the FG and MB approach, the absolute difference is computed as

$$\Delta_{SOC} = |SOC_{MB} - SOC_{FG}|. \quad (3.2)$$

3.2 Conduction-Only Heat Transfer

This section will discuss the comparisons of the FG and switched MB frameworks by only incorporating the effects due to conductive heat transfer. The final proposed model will capture the effects of natural convection in the liquid region of the PCM beginning in Section 3.3.

3.2.1 Complete Freezing and Melting

One complete cycle of the freezing and melting process goes through a normal operation for a TES, going through the FSM modes in ascending order. After going through all four modes, the end of a cycle happens when the last switch from Mode 4 to Mode 1 is made.

Table 3.1. Simulation Parameters

Variable	Description	Value	Units
T_{air}	Air Temperature	18	$^{\circ}C$
T_{sat}	Saturation Temperature	0	$^{\circ}C$
\dot{m}_{wf}	Mass Flow Rate	0.10	kg/s
$C_{p,wf}$	Specific Heat ($R - 134a$)	3.2	$kJ/(kg^{\circ}C)$
h_{wf}	Convective Heat Transfer Coeff. ($R - 134a$)	10^4	$W/(m^2^{\circ}C)$
ρ_{wf}	Density ($R - 134a$)	1200	kg/m^3
$C_{p,inn.}$	Specific Heat (Cu)	0.39	$kJ/(kg^{\circ}C)$
$k_{inn.}$	Thermal Conductivity (Cu)	401	$W/(m^{\circ}C)$
$\rho_{inn.}$	Density (Cu)	8960	kg/m^3
h_f	Heat of Fusion	334	kJ/kg
$C_{p,S}, C_{p,L}$	Specific Heat (Solid, Liquid)	2.11, 4.18	$kJ/(kg^{\circ}C)$
ρ_S, ρ_L	Density (Solid, Liquid)	916, 1000	kg/m^3
k_S, k_L	Thermal Conductivity (Solid, Liquid)	2.3, 0.58	$W/(m^{\circ}C)$
h_{air}	Convective Heat Transfer Coeff. (air)	25	$W/(m^2^{\circ}C)$
L	Length of pipe	1.00	m
$C_{p,out.}$	Specific Heat (PVC)	0.88	$kJ/(kg^{\circ}C)$
$k_{out.}$	Thermal Conductivity (PVC)	0.20	$W/(m^{\circ}C)$
$\rho_{out.}$	Density (PVC)	1350	kg/m^3
r_1	Inner Wall Radius	6.0	mm
r_5	Outer Wall Radius	28.8	mm
$\Delta r_{inn.}$	Inner Wall Thickness	0.8	mm
$\Delta r_{out.}$	Outer Wall Thickness	6.4	mm
Δr_{PCM}	PCM Thickness	19.1	mm
Δr	Difference in PCM radii	0.55	mm
M_{tot}	Total mass of PCM	1.90	kg

Fig. 3.1 shows the simulation results for the FG and MB models for two complete freezing and melting cycles. The top left plot shows trajectories for the simulated SOC using the FG and MB models, denoted SOC_{FG} and SOC_{MB} , while the top right plot shows Δ_{SOC} . Notably, the maximum and average values of Δ_{SOC} are 0.05 and 0.03, with the total computation of 1.2 seconds for the MB model and 6.1 seconds for the FG model. The lower left plot in Fig. 3.1 shows the mode switching for the MB model and the lower right plot

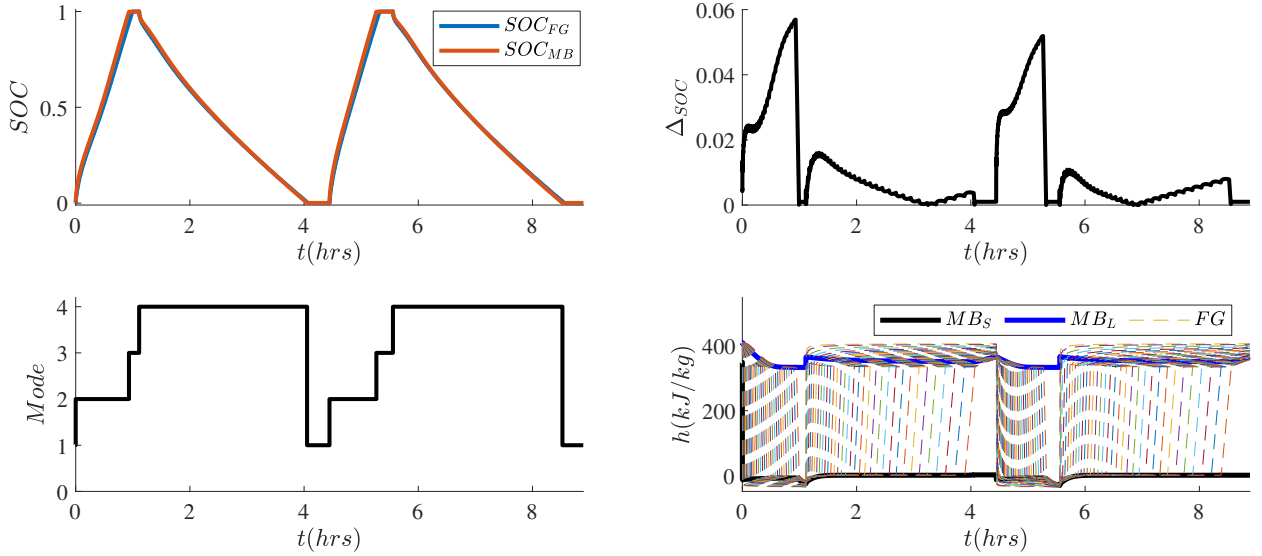


Figure 3.1. Differences between FG (with $n = 35$) and MB models for two complete freezing and melting cycles.

shows the solid and liquid region enthalpies for the MB model and all $n = 35$ enthalpies of for the PCM of the FG model. While simulating roughly five times faster than the FG model, the MB model is remarkably accurate when simulating complete freezing and melting cycles.

3.2.2 Partial Freeze-Melt Cycle

Fig. 3.2 shows how the MB approach loses accuracy when simulating partial freezing and melting of the PCM. When switching between Modes 2 and 4, the maximum value of Δ_{SOC} increases significantly up to 0.25. This is due to the fact that partial freezing can create complex geometries with multiple regions of solid and liquid. This complex geometry, which results in additional heat transfer surface area between the solid and liquid regions, cannot be captured by the conduction-only proposed MB model. This is why the SOC decreases significantly faster using the FG model during the first period of operation in Mode 4. Note that the accuracy of the MB increases on average when the PCM freezes completely in

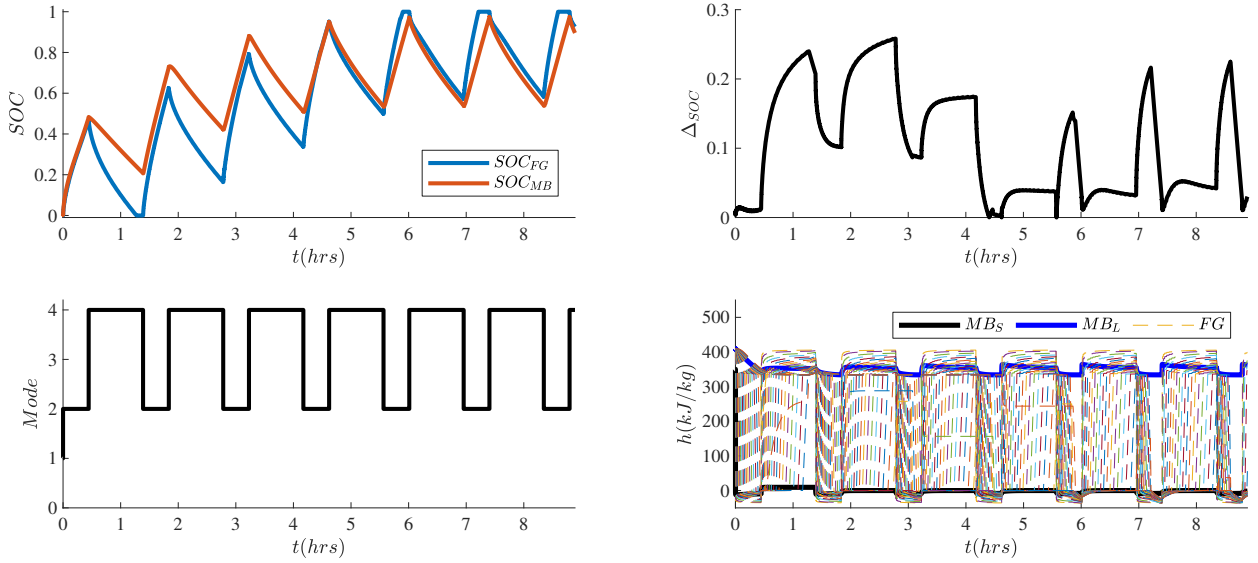


Figure 3.2. Differences between FG (with $n = 35$) and MB models for six partial freezing and melting cycles.

the latter half of the simulation. In summary, the conduction-only proposed MB modeling approach is only recommended when complete freezing and melting of the PCM is expected and Section 3.3 will focus on modifying the MB formulation to more accurately capture behavior associated with partial freezing and melting.

3.3 Final Proposed Model

The final FG and proposed switched MB models incorporate natural convection and the surface area ratio from Sections 2.3.4 and 2.3.5. This will be used to validate against the experimental setup in Chapter 4, but comparisons in the partial freezing and melting cases are made between the FG and switched MB models in this section.

3.3.1 Partial Freeze-Melt Cycle

The results in Fig. 3.3 show the importance of including the surface area ratio, γ , from Section 2.3.5 when the system operation results in partial freezing and melting of the PCM.

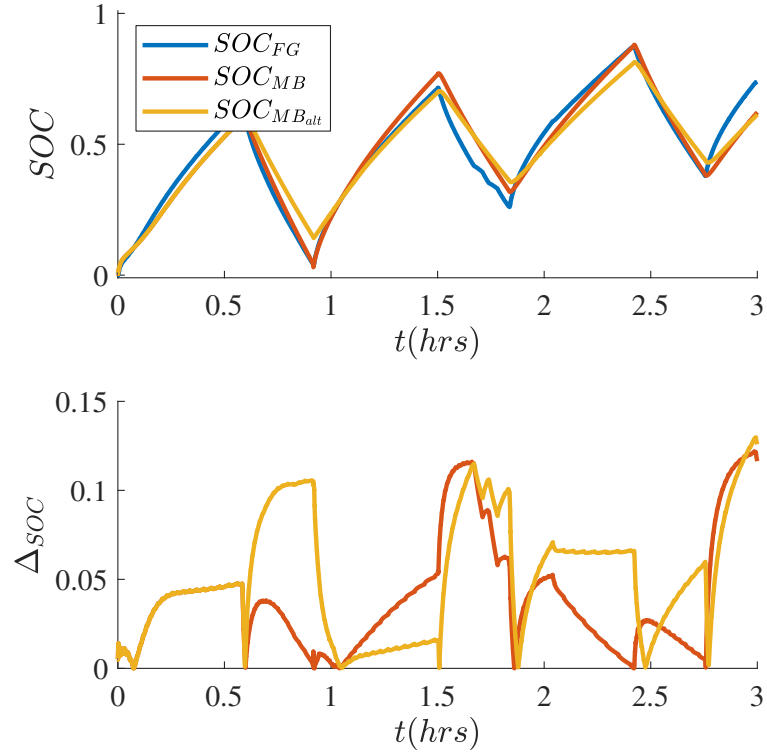


Figure 3.3. Differences between FG (with $n = 35$) and MB models for six partial freezing and melting switches. This MB model incorporates $\gamma = 2$ after the first switch.

Here, MB_{alt} refers to the proposed model with $\gamma = 1$, while MB refers to the proposed model with $\gamma = 2$. As seen in Fig. 3.3, the surface area ratio has the ability to significantly improve the accuracy of the MB model, as seen by the significant reduction in Δ_{SOC} between 0.5 and 1 hour. Note that the MB model is not always more accurate than MB_{alt} , as seen in the operation around 1.5 hours. However, overall, the inclusion of the surface area ratio reduced the average Δ_{SOC} from 0.0474 when using $\gamma = 1$ to 0.0372 when using $\gamma = 2$, leading to a 21% reduction in the average Δ_{SOC} .

CHAPTER 4

EXPERIMENTAL STUDY

4.1 Experimental Setup

4.1.1 Experimental System Overview

The experimental setup used to validate the proposed MB model operates using a R134a Vapor Compression System (VCS) to either store or extract thermal energy from the TES. The five core components are the compressor, condenser, electric expansion valves, evaporator (cold-plate resistive heater) and the TES device, as shown in Fig. 4.1. Fig. 4.2 provides a system diagram that includes major components and sensors. Table 4.1 provides identifying part numbers for key components of the system.

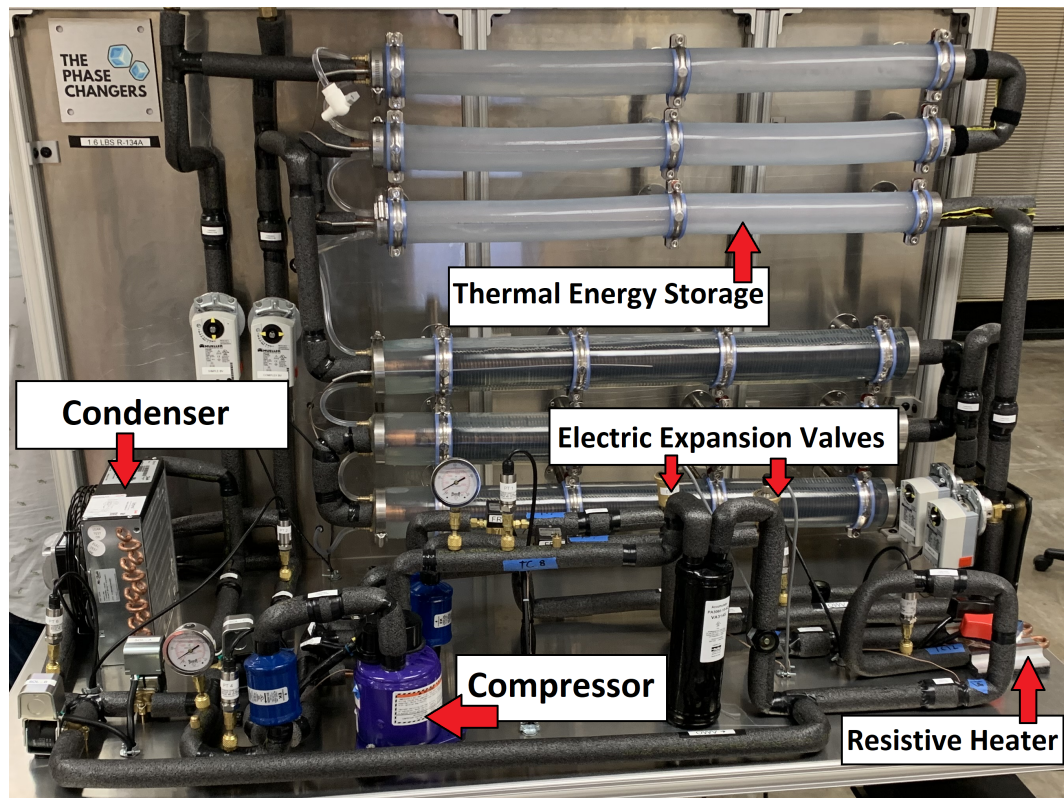


Figure 4.1. Experimental system with core components labeled.

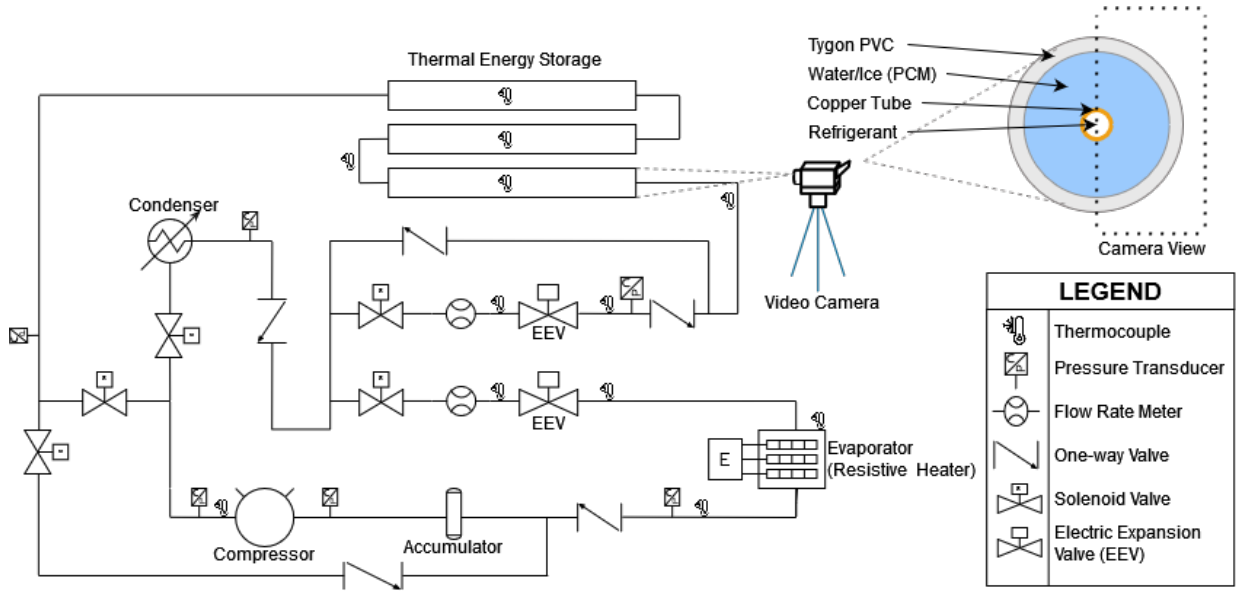


Figure 4.2. Diagram of the experimental VCS from Fig. 4.1 with three TES devices in series.

4.1.2 TES Description

The TES device consists of three identical sections in series, where only the first section is considered in the experimental validation of the proposed model. The TES is charged when acting as an evaporator in a vapor compression cycle and is discharged when acting as a condenser, as shown in Fig. 4.3. The outer cylindrical pipe material was chosen to be elastic to handle the volumetric changes associated with the water-ice phase transition. The dimensions of the experimental TES are provided in Table 3.1 and are used as parameters in the FG and MB models.

4.1.3 Data Processing

A Speedgoat Performance real-time target machine and Simulink-Realtime are used for data acquisition and system control. Type-T surface mount thermocouples ($\pm 1.00^\circ\text{C}$ or $\pm 0.75\%$) at the inlet and outlet of the TES verify that the copper pipe through the TES is isothermal due to two-phase heat transfer. In refrigeration terms the TES section has no super-heat

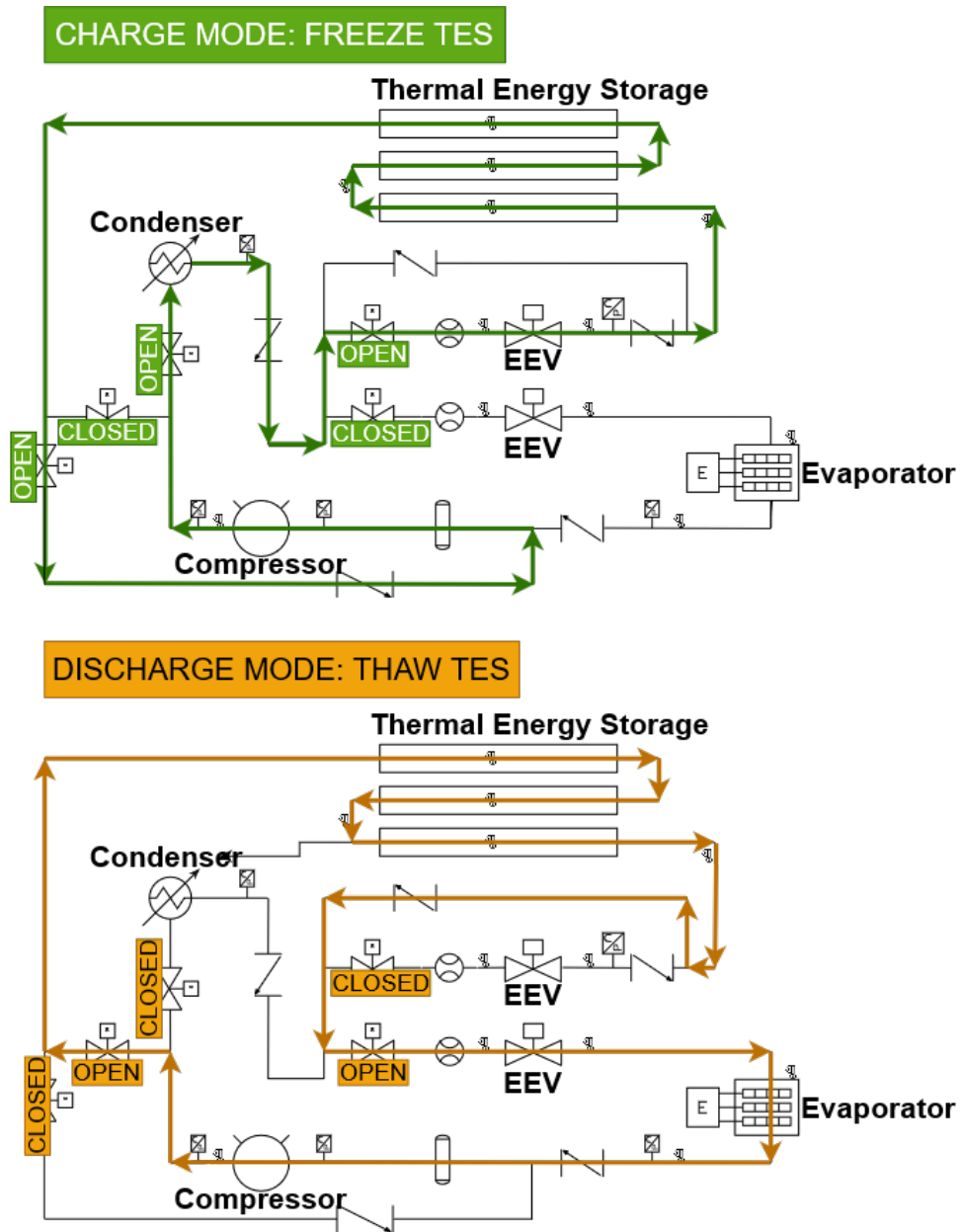


Figure 4.3. System configuration and flow directions for the charge (top figure) and discharge (bottom figure) modes of TES operation.

Table 4.1. System Components

Common Name	Manufacturer	Identifying Code	Quantity
Compressor	Masterflux	Sierra00163	1
Condenser	Danfoss	114N2022	1
Expansion Valve	Sporlan	SERAA10S-3X4	2
Resistor (Evaporator)	Ohmite	TA2K0PH5ROOKE	1
Heat Sink (Evaporator)	Ohmite	CP4A-114C-108E	1
Power Supply (Evaporator)	B&K Precision	1901B	1
Accumulator	Parker	VA314S	1
Solenoid Valve	Danfoss	EVR6	3
Solenoid Coil	Danfoss	BJ120CS	3
Solenoid Valve	Parker	R16E33	2
Solenoid Coil	Parker	T2F	2
Flow Meter	McMillan	102-5-D-B4-H	2
Thermocouple-T	McMaster	9251T71	10
Immersion	McMaster	3857K58	3
Thermocouple-T			
Pressure Sensor	Omega	PX309-500A10	6
Camera	Sony	ZV-1F	1
DAQ	Speedgoat	Serial 7355	1

when acting as an evaporator and no sub-cool when acting as a condenser. A Sony ZV-1F camera was used to collect video data of the TES to estimate SOC. Fig. 4.4 shows the view obtained by the camera. A full view of the TES is obstructed by the copper pipe, therefore only the right half of the TES is analysed with the assumption of symmetry about the vertical axis. Video recordings of the TES are sampled to form a set of discrete images and timestamps. The isothermal property simplifies SOC calculation into two dimensions. SOC is calculated as the ratio of the area of ice to the area of the phase change material region. To find these areas, the regions are manually traced using MATLAB's `drawpolygon` and `polyarea` functions.

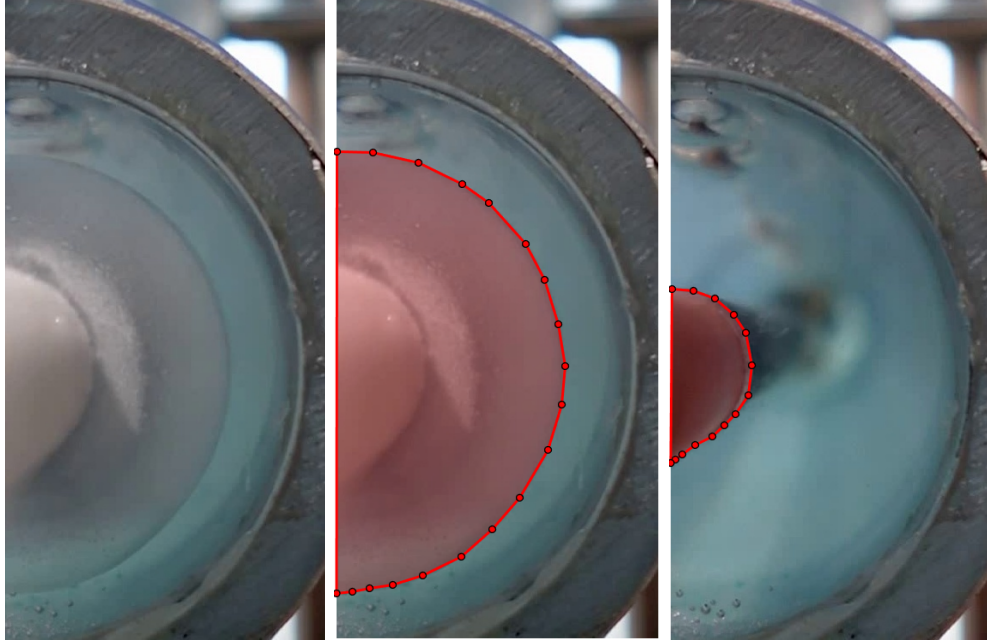


Figure 4.4. Sample images of TES with region tracing. LEFT: View of TES in freeze cycle. MIDDLE: The region in red is traced over the water-ice boundary from the left image. RIGHT: The region in red traces the copper pipe. This area is subtracted off from the ice area when the view of the copper pipe is obstructed by frost.

4.2 Experimental Validation

The simulated FG and switched MB models will incorporate natural convection in these comparisons to the experimental system data.

4.2.1 Comparison of Mode 1

The first experiment is designed to operate the system entirely in Mode 1 to experimentally determine the heat transfer coefficient h_{air} and the corresponding thermal resistance due to natural convection between the outer wall and surrounding air (R_{air}) from (2.9).

As shown in Fig. 4.5, the VCS is operated so that the inlet refrigerant (working fluid) temperature to the TES device stays above $T_{sat} = 0^\circ\text{C}$ for the PCM. With this relatively high inlet temperature, there is a large difference between the inlet and outlet temperatures of the working fluid, which violates assumption 1 from Section 2.2.1 of uniform heat transfer along

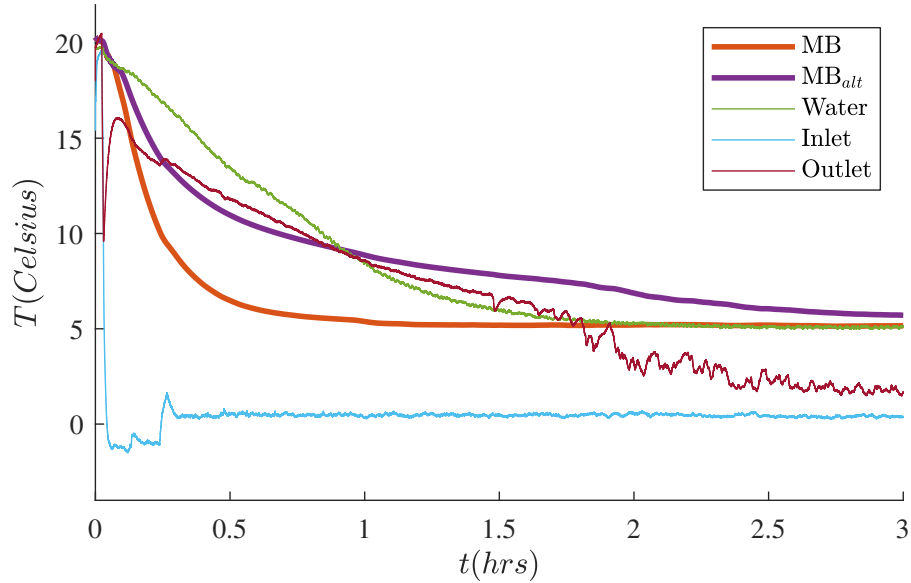


Figure 4.5. Comparison of the water temperature of the experimental system and the MB model while in Mode 1 of operation.

the length of the TES device. Therefore, Fig. 4.5 shows the results of two different models: 1) MB, where the inlet temperature to the model equals the experimentally measured inlet temperature and 2) MB_{alt} , where the inlet temperature to the model equals the average of the experimentally measured inlet and outlet temperatures.

The main result of this experiment is that modeling $h_{air} = 25W/(m^2C)$, corresponding to $R_{air} = 200.4C/W$, results in the same steady-state simulated (red trace) and experimental (green trace) water temperatures, as shown in Fig. 4.5. While these steady-state temperatures match, it is important to note the differences in the transient behavior. The slightly improved fit of MB_{alt} (purple trace) suggests part of this discrepancy may be due to the non-uniform heat transfer along the length of the TES due to the varying working fluid temperature. The remaining differences may be attributed to the fact the experimental water temperature measurement is from a single thermocouple located near the outer pipe, while the temperature from the MB model represents the lumped average temperature of all of the water in the TES.

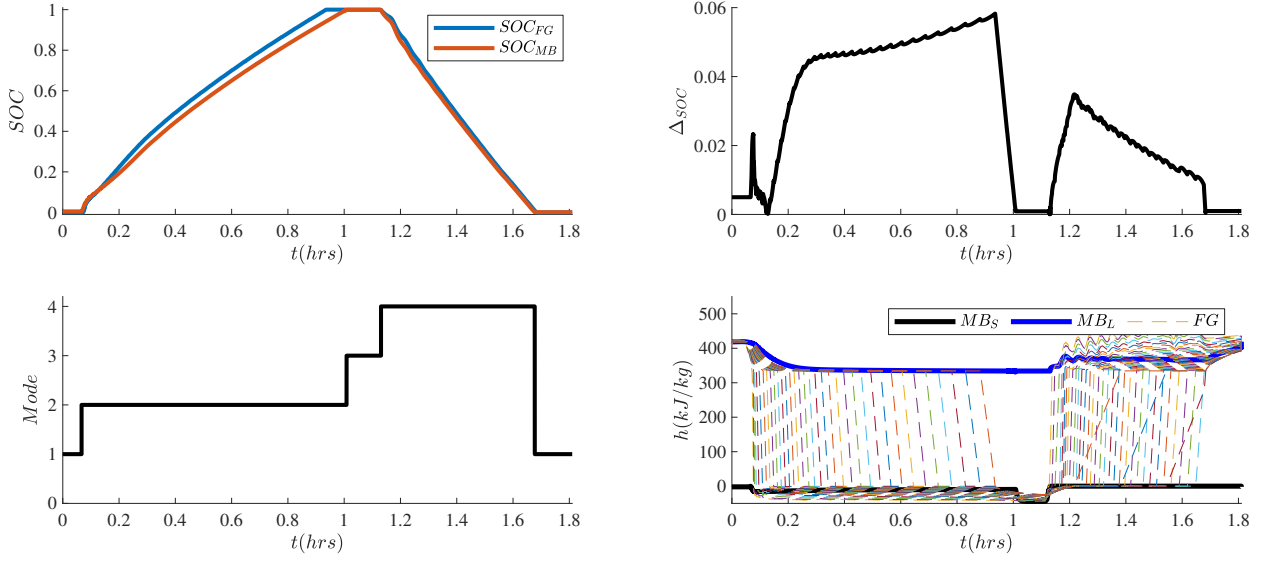


Figure 4.6. Differences between FG (with $n = 35$) and MB models for one complete freezing and melting cycle.

4.2.2 Complete Freeze-Melt Cycle

Fig. 4.6 shows the simulation results for the FG and MB models for one complete freezing and melting cycle. The top left plot shows trajectories for the simulated SOC using the FG and MB models, denoted SOC_{FG} and SOC_{MB} , while the top right plot shows Δ_{SOC} . Notably, the maximum and average values of Δ_{SOC} are 0.06 and 0.03. The lower left plot in Fig. 4.6 shows the mode switching for the MB model and the lower right plot shows the solid and liquid region enthalpies for the MB model and all $n = 35$ enthalpies of for the PCM of the FG model. Simulation times for the FG and MB models are 13.8 and 3.4 seconds, respectively, with the MB model simulating roughly 1800 times faster than real-time. In freezing mode, the average $k_{eq} = 5.0$, corresponding to $Ra = 3.76 \times 10^5$. In melting mode, the average $k_{eq} = 3.4$, corresponding to $Ra = 8.00 \times 10^4$.

Fig. 4.7 compares the results from the MB, FG, and experimental system for one complete cycle, along with examples of four images used to estimate SOC based on the approach presented in Fig. 4.4. The experimental system data set trajectories are provided in Fig. 4.8

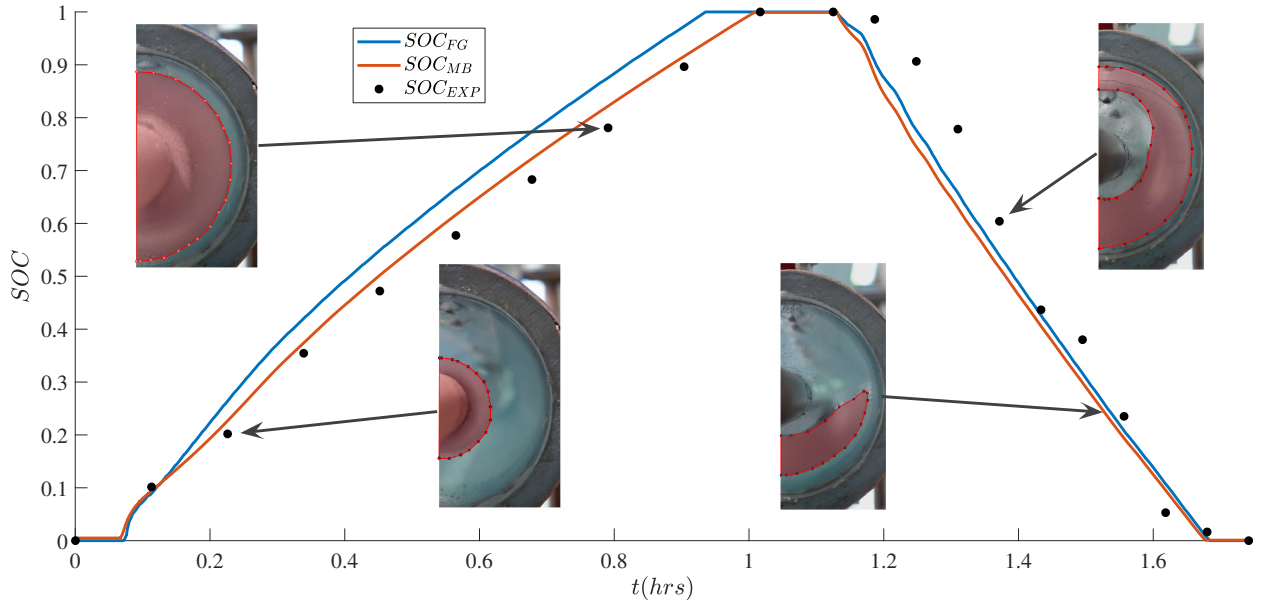


Figure 4.7. Comparison of the SOC from the experimental TES data, MB simulation, and FG simulation with images

for the PCM (water) and working fluid inlet and outlet temperatures. Note the similarities between the inlet and outlet working fluid temperatures during the majority of the experiment, which supports the assumption of uniform heat transfer along the length of the TES. However, during the first 30 minutes of the experiment the outlet working fluid temperature is significantly higher than the inlet temperature, and this is not directly accounted for in the model.

Overall, SOC is experimentally estimated using ten images of the TES for both the freezing and melting modes. The MB model estimates the total freezing and melting time of the experimental system within approximately 61 and 226 seconds, respectively. During the freezing and melting processes, the average difference in SOC between the MB and experimental data across both Modes 2 and 4 are measured as 0.0268 and 0.0765, respectively.

The results in Fig. 4.9 demonstrate the importance of accounting for natural convection through the use of k_{eq} . While the experimental (black dots) and MB model (red trace) are the same as in Fig. 4.7, the MB_{alt} (green trace) is the result of the conduction-only MB

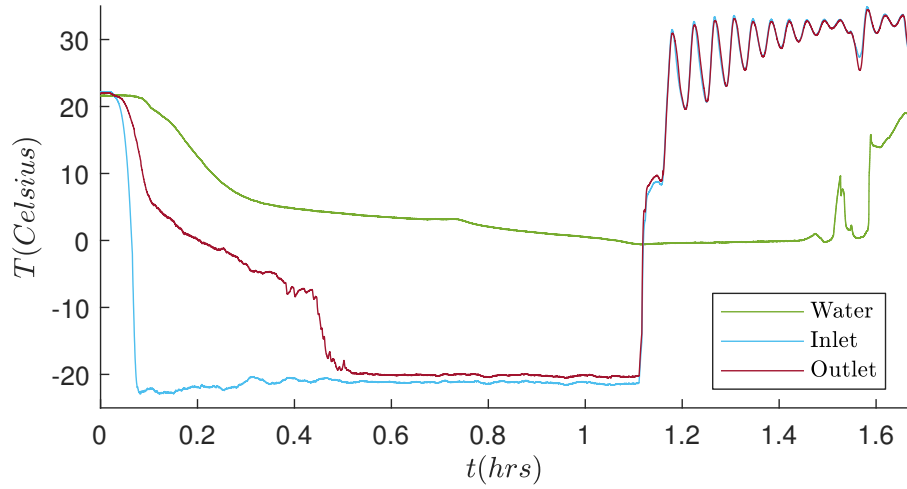


Figure 4.8. Input temperatures for the complete freezing and melting cycle

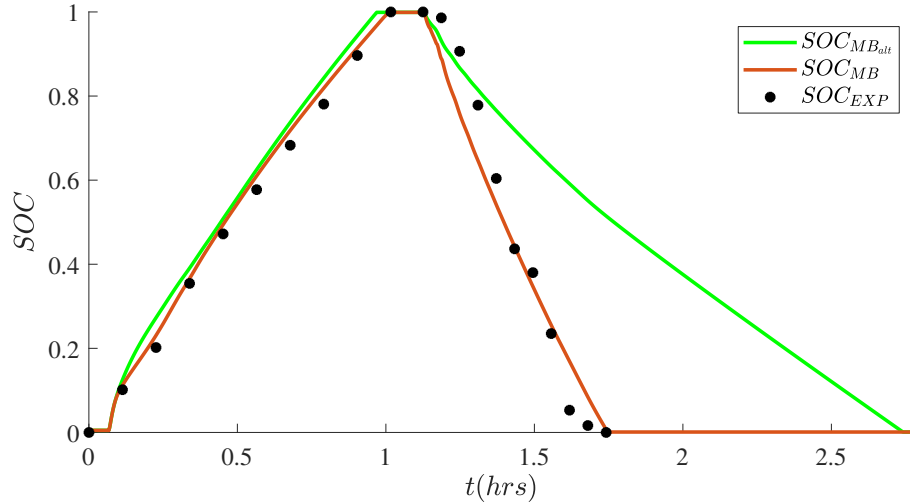


Figure 4.9. Difference between using k_{eq} to account for natural convection in water to match experimental data compared to the conduction model presented in Section 3.2.1.

model from Section 3.2, where $k_{eq} = 1$. Interestingly, accounting for natural convection only slightly affects the SOC trajectory while the TES is freezing. This is likely due to the fact that the majority of the heat transfer within the TES is between the working fluid, inner pipe, and solid region of the PCM, which is governed by conduction. However, including k_{eq} reduces the melting time by 67%, resulting in significantly better agreement between the proposed model and experimental data.

CHAPTER 5

CONCLUSIONS AND FUTURE WORK

This thesis presented an experimentally validated switched moving boundary approach for modeling thermal energy storage devices with a phase change material. Graph-based modeling was used to identify the structure of the dynamics when using a fixed grid and the proposed moving bounding modeling approaches. A finite state machine allowed the moving boundary model to switch modes to capture the dynamics associated with freezing, melting, completely solid, and completely liquid phase change material. A conduction-only approach was compared to the traditional fixed grid approach for model accuracy before being compared to experimental data. Effects due to natural convection in the liquid region of the phase change material were captured using a mean equivalent conductivity coefficient. A surface area ratio was used to account for complex geometries formed from partial freezing and melting cases. Experimental results demonstrated the accuracy of the proposed switched moving boundary model and the importance of modeling the effects of natural convection.

Future work in switched moving boundary modeling should focus on experimental validation of the approach for different types of TES devices and experimental systems. To confirm the accuracy of the current switched moving boundary model, testing the model against different thermal energy storage geometries will be useful to confirm the accuracy of the model on a larger scale. The geometries to test can be based on shape of the device or the amount of heat transfer area available for use by the device. The shape can be different from the cylindrical shape tested in this thesis, such as rectangular prisms or other geometrical shapes. The amount of heat transfer area can change simply by the size of pipes used, but the main interesting change could be using a thermal energy storage device that incorporates a large array of pipes connected in parallel to increase the surface area between the working fluid and the phase change material.

Using the control-oriented switched moving boundary model to develop and implement control strategies for thermal energy storage devices is another avenue for further research. While the results of this thesis show that relatively few dynamic states can accurately model the state of charge of a thermal energy storage device, it is important for future work to study how these models can be used to optimize the freezing and melting of the phase change material to maximize the performance and efficiency of the overall thermal management system.

REFERENCES

- Agarwal, N., F. Chiara, and M. Canova (2012). Control-oriented modeling of an automotive thermal management system. In *The International Federation of Automatic Control*.
- Amagour, M. E. H., M. Bennajah, and A. Rachek (2021). Numerical investigation and experimental validation of the thermal performance enhancement of a compact finned-tube heat exchanger for efficient latent heat thermal energy storage. *Journal of Cleaner Production* 280, 124238.
- Bergman, T. L. and F. P. Incropera (2011). *Fundamentals of Heat and Mass Transfer, Seventh Edition*. Wiley.
- Bird, T. J. and N. Jain (2020). Dynamic modeling and validation of a micro-combined heat and power system with integrated thermal energy storage. *Applied Energy* 271, 114955.
- Chen, P. and J. Wang (2014). Control-oriented model for integrated diesel engine and aftertreatment systems thermal management. *Control Engineering Practice* 22, 81–93.
- Dede, A., D. D. Giustina, G. Massa, M. Pasetti, and S. Rinaldi (2016). A smart pv module with integrated electrical storage for smart grid applications. In *International Symposium on Power Electronics, Electrical Drives, Automation and Motion*.
- Fasl, J. M. and A. G. Alleyne (2013). Modeling and control of hybrid vapor compression cycles. Master’s thesis, University of Illinois at Urbana-Champaign.
- Fortunato, B., S. M. Camporeale, M. Torresi, and M. Albano (2012). Simple mathematical model of a thermal storage with pcm. *AASRI Procedia* 2, 241–248.
- Francis, N. D., M. T. Itamura, S. W. Webb, and D. L. James (2002). Cfd calculation of internal natural convection in the annulus between horizontal concentric cylinders. *Sandia National Laboratories*, SAND–2002–3132.
- Frazzica, A., M. Manzan, and et. all (2022). Experimental validation and numerical simulation of a hybrid sensible-latent thermal energy storage for hot water provision on ships. *Energies* 15, 2596.
- Ghaeminezhad, N., Z. Wang, and Q. Ouyang (2023). A review on lithium-ion battery thermal management system techniques: A control-oriented analysis. *Applied Thermal Engineering* 219, 119497.
- Kuehn, T. H. and R. J. Goldstein (1976). An experimental and theoretical study of natural convection in the annulus between horizontal concentric cylinders. *Journal of Fluid Mechanics* 74, 695–719.

- Laird, C. E. and A. G. Alleyne (2019). A hybrid electro-thermal energy storage system for high ramp rate power applications. In *Dynamic Systems and Control Conference*.
- Laird, C. E. and A. G. Alleyne (2021). Modeling, control, and design of hybrid electrical and thermal energy storage systems. Master’s thesis, University of Illinois at Urbana-Champaign.
- Lee, D., R. Ooka, S. Ikeda, W. Choi, and Y. Kwak (2020). Model predictive control of building energy systems with thermal energy storage in response to occupancy variations and time-variant electricity prices. *Energy and Buildings* 225, 110291.
- Ma, Y., A. Kelman, A. Daly, and F. Borrelli (2012). Predictive control for energy efficient buildings with thermal storage: Modeling, stimulation, and experiments. *IEEE Control Systems* 20, 796–803.
- Nazir, H., M. Batool, and et al. (2019). Recent developments in phase change materials for energy storage applications: A review. *International Journal of Heat and Mass Transfer* 129, 491–523.
- Pangborn, H. C., A. G. Alleyne, and N. Wu (2015). A comparison between finite volume and switched moving boundary approaches for dynamic vapor compression system modeling. *International Journal of Refrigeration* 53, 101–114.
- Pangborn, H. C., C. E. Laird, and A. G. Alleyne (2020). Hierarchical hybrid mpc for management of distributed phase change thermal energy storage. In *American Control Conference*.
- Shanks, M. A. and N. Jain (2022). Design, control, and validation of a transient thermal management system with integrated phase-change thermal energy storage. Master’s thesis, Purdue University.
- Sharma, A., V. Tyagi, C. Chen, and D. Buddhi (2009). Review on thermal energy storage with phase change materials and applications. *Renewable and Sustainable Energy Reviews* 13, 318–345.
- Wang, W. and J. P. Koeln (2020). Hierarchical multi-timescale energy management for hybrid-electric aircraft. In *Dynamic Systems and Control Conference*.
- Wang, Y., J. Chen, and W. Zhang (2019). Natural convection in a circular enclosure with an internal cylinder of regular polygon geometry. *AIP Advances* 9, 065023.
- Zalba, B., J. M. Marin, L. F. Cabeza, and H. Mehling (2003). Review on thermal energy storage with phase change: materials, heat transfer analysis and applications. *Applied Thermal Engineering* 23, 251–283.

Zhang, K., M. Yang, and Y. Zhang (2014). Two- and three-dimensional numerical simulations of natural convection in a cylindrical envelope with an internal concentric cylinder with slots. *International Journal of Heat and Mass Transfer* 76, 190–199.

BIOGRAPHICAL SKETCH

Trent J. Sakakini grew up in Frisco, Texas, and he attended The University of Texas at Dallas, where he completed his Bachelor of Science in Mechanical Engineering in 2021. He continued at UTD to work for his Master of Science in Mechanical Engineering, expecting to graduate in May of 2023. Throughout his time at UTD, he was inducted into Tau Beta Pi, an engineering honors society where only the top eighth of the junior or top fifth of the senior classes are inducted. Additionally, he was a member of the NCAA Division III Cross Country and Track and Field teams, where he earned three team Cross Country titles (2018, 2019, and 2020) as well as five individual Track titles in the 800 meters (2022 and 2023), 1500 meters (2022), and 3000 meter Steeplechase (2022 and 2023) while competing in the American Southwest Conference. After completing his MS degree, he will be joining Lockheed Martin as a Guidance, Navigation, and Controls Engineer.

CURRICULUM VITAE

Trent J. Sakakini

May 4, 2023

Contact Information:

Department of Mechanical Engineering Email: trent@utdallas.edu
The University of Texas at Dallas
800 W. Campbell Rd.
Richardson, TX 75080-3021, U.S.A.

Educational History:

BS, Mechanical Engineering, The University of Texas at Dallas, 2021
MS, Mechanical Engineering, The University of Texas at Dallas, expected 2023

Employment History:

Research Assistant, UTD Energy Systems Control Laboratory, September 2021 – present
Vehicle Integration Intern, Northrop Grumman, May 2022 – August 2022
Advanced Technology Intern, Lennox International, June 2021 – August 2021
Engineering Intern, Cobalt Product Solutions, November 2020 – January 2021
Engineering Intern, First Company, June 2019 – August 2019

Professional Recognitions and Honors:

Outstanding Teaching Assistant Award, Mechanical Engineering, UTD, 2022
Distinguished Scholar-Athlete, American Southwest Conference, 2022
Outstanding Track Athlete, American Southwest Conference, 2022
Student Design Manufacturing Competition (2nd place), ASME, 2021
Graduated *magna cum laude*, UTD, 2021

Professional Memberships and Activities:

Tau Beta Pi (TBP), 2020–present
NCAA DIII Men's Cross Country and Track & Field, UTD, 2018–2023